Piezo-photocatalysts based on a ferroelectric high-entropy oxide

Shun Cheng Chang [a,1], Hsuan-Yu Chen [a,1], Po-Han Chen [a], Jyun-Ting Lee [a], Jyh Ming Wu [a,b,*]

[a] Department of Materials Science and Engineering, National Tsing Hua University, 101, Section 2 Kuang Fu Road, Hsinchu 300, Taiwan
[b] High Entropy Materials Center, National Tsing Hua University, 101, Section 2 Kuang Fu Road, Hsinchu 300, Taiwan

ARTICLE INFO

ABSTRACT

We develop a porous ferroelectric high-entropy oxide (HEO) by tuning the Ca concentration in $(Ca_xZrYCeCr)O_2$ ($x = 0.09$–0.5). Time-resolved photoluminescence indicates that the ferroelectric HEO sample containing 38 at% Ca atoms (38HEO) exhibits a long carrier lifetime of approximately 66 ns, 163% of the lifetime of $Zr_{0.3}Y_{0.3}Ce_{0.3}Cr_{0.09}O_2$. The theoretical calculation reveals that the porous HEO into which ferroelectric $Ca(Zr_{0.95}Cr_{0.5})O_3$ nanoparticles are embedded, separating electron-hole pairs efficiently and provides trapping centers in the piezocatalytic process, considerably prolonging the carrier lifetime. The reaction rate constant of 38HEO for the decomposition of dye molecules is 1000% of that for pristine $ZrYCeCrO_2$. The hydrogen evolution reaction with polarized 38HEO resulted in hydrogen production of 677 $\mu molg^{-1}h^{-1}$, 163% that of unpolarized 38HEO. The piezopotential of the ferroelectric $Ca(Zr_{1-x}Cr_x)O_3$ was strongly coupled with the charge transfer of the HEO's surface, enhancing the catalytic activity. The concepts reported herein can be used to design next-generation piezo-photocatalysts.

1. Introduction

Photoelectrochemical reactions have considerable scope for application to water splitting and water purification [1–3]. Nevertheless, developing photocatalysts with high quantum yield remains challenging owing to the low conversion efficiency of such catalysts. In this context, creating heterojunctions and cocatalysts [4–6], single-atom catalysts [7], cooperative catalysis coupling effect [8–11], introducing energy levels by forming oxygen vacancies, and charge compensation are promising methods that have been considered for reducing the ease of electron–hole recombination. Furthermore, aside from utilizing solar energy as a resource, scholars have developed diverse energy-harvesting methods [12], including the use of piezoelectric [13,14], pyroelectric [15], ferroelectric [16–18], and few-layered two-dimensional transition-metal dichalcogenide materials (TMDs)[19–21] for producing H_2 gas and treating water pollutants in a dark environment through a mechanical-strain-induced piezoelectric potential (piezopotential). [22–24] In addition, piezopotentials have been effectively modulated by modifying the concentration of oxygen vacancies in ferroelectric nanostructures [25–28]; such vacancies play a vital role in the piezocatalytic process [29–33].

Piezopotentials can be used to tune the carrier concentration at the interface of heterostructures, and defects introduce trap energy levels in the bandgap and suppress nonradiative and radiative electron-hole recombination [33–35]. When coupled with the photocatalytic effect, a piezopotential can dramatically accelerate the charge transfer process, thereby enhancing the efficiency of a photocatalyst [36–38]. Accordingly, in this work, we proposed that the high-entropy oxides (HEOs) have beneficial catalyst characteristics such as slow diffusion dynamics, lattice distortion, and scope for defect engineering. This study employed ceria-zirconia, which has a cubic fluorite structure containing five or more different metal cations in single-phase and multiphase HEO structures to reduce the normal bandgap energy of the material. Substituting Zr^{+4} and Ce^{+4} with Y^{3+} and Cr^{3+}, respectively, to form a $ZrYCeCrO_2$-based compound yielded a broad visible-light absorbance range with multiple electron-trapping states corresponding to Zr^{+4}, Y^{+3}, Ce^{+4}, Cr^{3+}, and oxygen vacancies in the band structure that play vital trapping centers for slow recombination rate effectively.

Considering the piezophototronic effect in the visible range, we combined a ferroelectric component with an HEO compound. Controlling the concentration of Ca ions precipitated a ferroelectric material $CaZr_{1-x}Cr_xO_3$ ($x \approx 0.05$) with the optimal concentration of oxygen vacancies. Notably, the built-in piezopotential arising from the ferroelectric polarization of $CaZr_{1-x}Cr_xO_3$ provided an electric field to inhibit
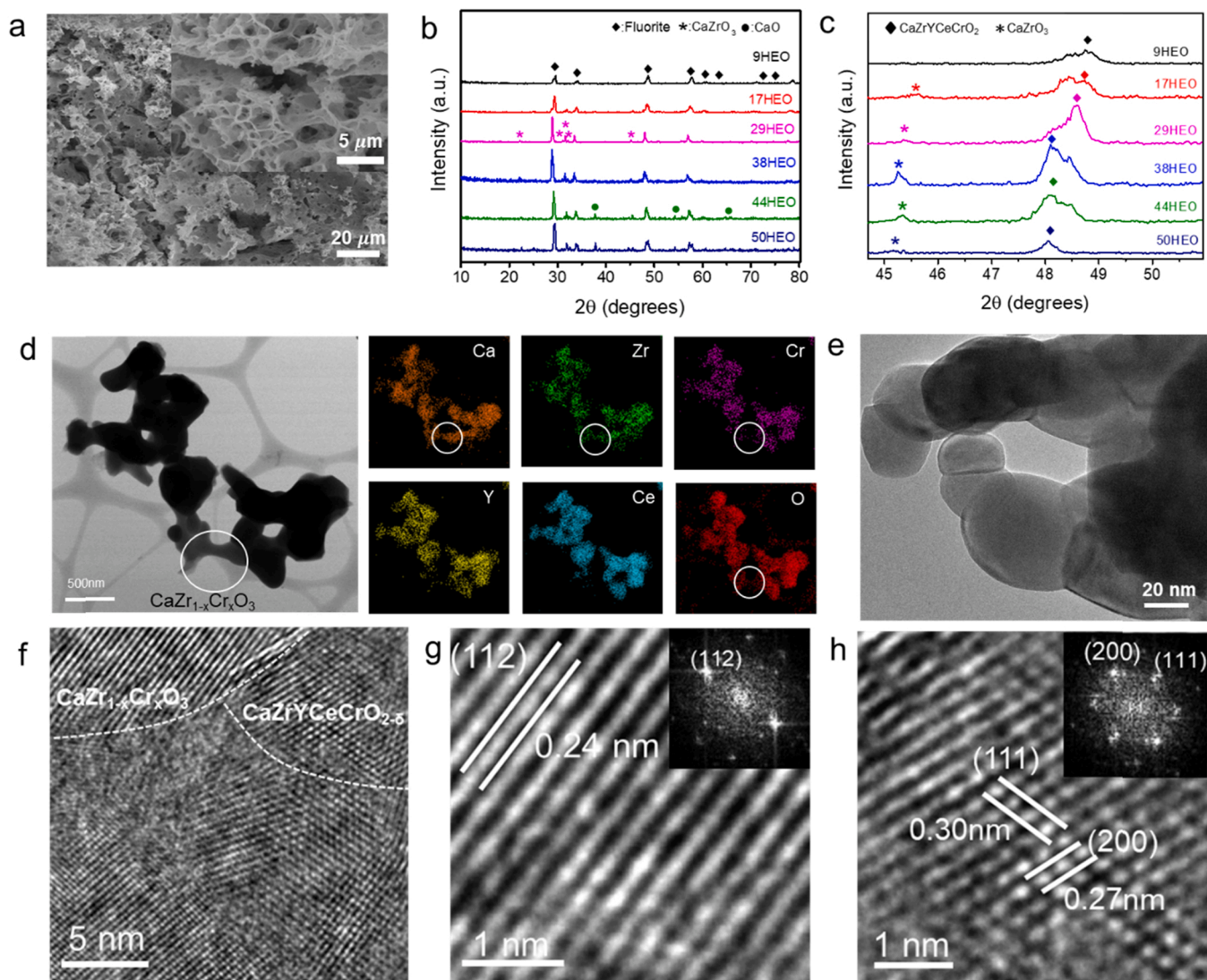
Fig. 1. (a) Low and high magnitude SEM image (inset) of HEO reveals porous morphology. (b)-(c) XRD patterns of HEO and excess calcium content of HEO, shifting toward a lower angle as increasing calcium concentration. (d) TEM image of HEO with EDS mapping of TEM image, showing that the Ca, Zr, Y, Ce, Zr, O are highly dispersed in HEO compounds. (e) The low magnification TEM image of the HEO. (f) TEM image of $Ca(Zr_{1-x}Cr_x)O_3$ and $CaZrYCeCrO_2$ forming a grain boundary. (g) HRTEM image of $Ca(Zr_{1-x}Cr_x)O_3$, inset is its corresponding FFT image. (h) HRTEM image of $CaZrYCeCrO_2$ (HEO), inset is its corresponding FFT image.

electron-hole pair recombination in the HEO catalyst. Theoretical calculations revealed that this inner electric field at interfacial phase boundaries effectively moderated free carriers, thereby enhancing the charge separation in the ferroelectric HEO catalyst. When an external mechanical force was coupled with photoirradiation, the photoinduced charge separation coupled with piezoelectric polarization enhanced the charge transport in trapping sites. This increased the carrier lifetime for the catalytic reaction, enhancing the electrochemical redox performance of the ferroelectric HEO substantially.

2. Experimental section

2.1. Synthesis of HEOs

$Ca_xZrYCeCrO_2$ (x = 0.09–0.5) samples were synthesized using a sol-gel method. First, metallic nitrate powders—$Ca(NO_3)_2 \cdot 4 H_2O$ (SHOWA, 98%), $ZrO(NO_3)_2 \cdot xH_2O$ (Sigma Aldrich, 99%), $Y(NO_3)_3 \cdot 6 H_2O$ (Alfa Aesar, 99.9%) $Cr(NO_3)_3 \cdot 9 H_2O$ (Acros Organics, 99%), and $Ce(NO_3)_3 \cdot 6 H_2O$ (Alfa Aesar, 99.5%)—were added to deionized water to obtain a precursor solution. Next, citric acid was slowly added to the solution as a chelating agent, and ammonia solution was added to adjust

the pH to 7. The molar ratio of the metallic nitrate to citric acid was 1:0.3. Finally, the solution was dried at 90 °C for 48 h in an oven to obtain a gel and then sintered at 1100 °C in the ambient atmosphere to prepare HEO powder. Subsequently, 100 mg of the as-synthesized dried gel was dissolved in 3 mL of 2% polyvinyl alcohol to obtain a solution, which was then spin-coated on a silicon substrate to form a thin film and sintered at 1100 °C for measuring the sample's ferroelectric property.

2.2. Material characterization

The crystal structure and surface morphology of the as-synthesized metal-oxide samples were investigated using HRTEM (JEOL, JEM-ARM200FTH), field-emission SEM (HITACHI SU8010), and XRD (Bruker D2). A Raman spectroscope (HORIBBA IHR-550) equipped with a He–Ne laser (532 nm) serving as an excitation source was used to observe the vibrational modes of atomic bonding interactions. X-ray photoelectron spectroscopy (Thermo Fisher Scientific, ESCALAB Xi$^+$) was employed to investigate the chemical state and phase composition of elements in the target materials. The piezoelectric response of the HEOs was measured through PFM (Bruker Dimension Icon). A PL spectrometer (Jobin Yvon/Labram HR) equipped with a He–Cd laser
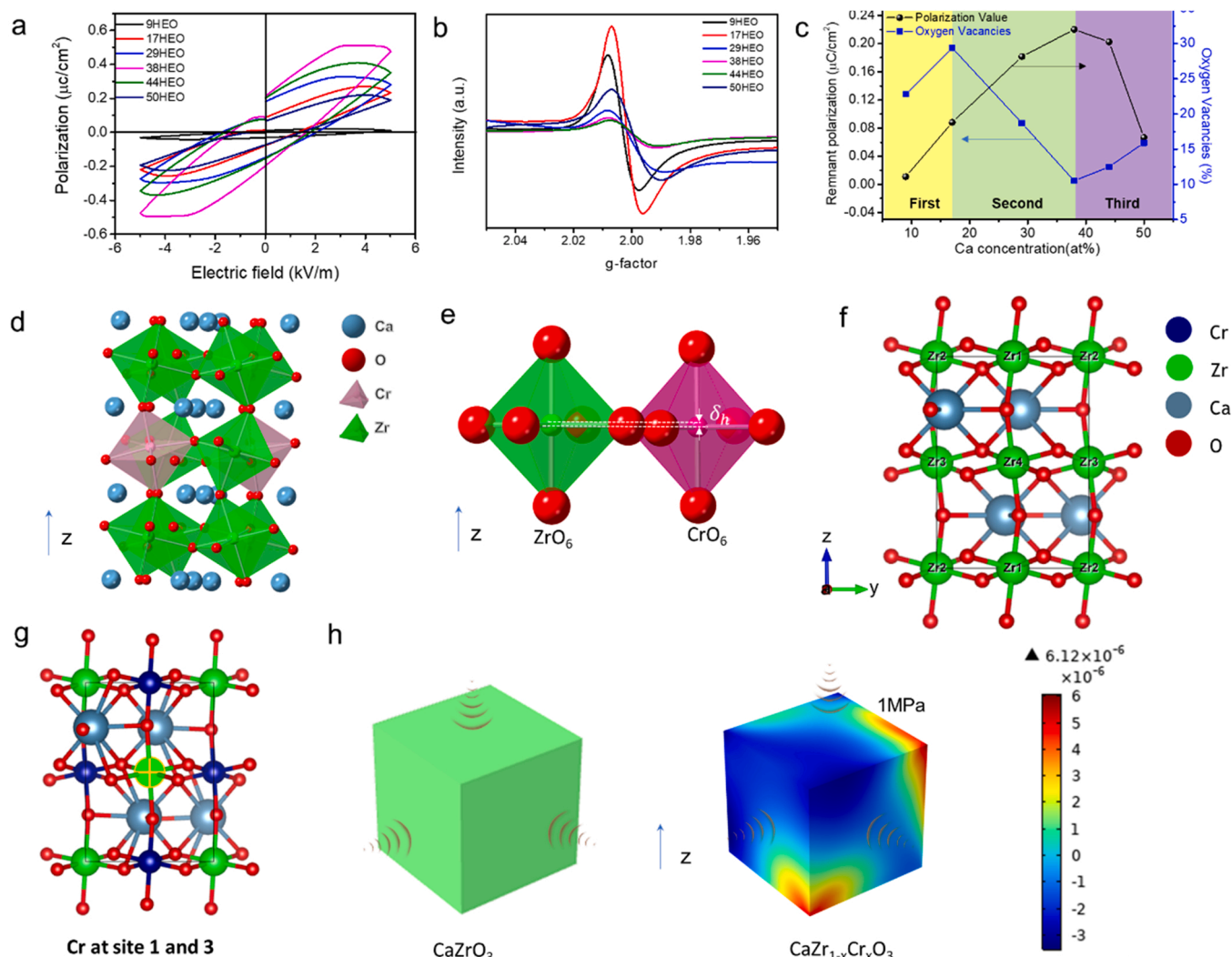
Fig. 2. (a) The P-E curves of the 9–50 HEO, (b) The corresponding EPR spectra of the spin concentration variations from the 9–50 HEO. The g factor = 2.006, denotes when the magnetic field is parallel to the c axis. (c) The value of polarization of HEO and concentration variations of oxygen vacancies (%) as a function of Ca content. (d) The crystallographic of $CaZr_{1-x}Cr_xO_3$. (e) The crystallographic ZrO_6 and CrO_6 show the Cr atom has deviated from the octahedron center by nonequivalent amounts along the z-axis. (f) The configuration of pristine $CaZrO_3$, and (g) The configuration of $CaZrO_3$:Cr that Cr occupied at site #1 and #3 (h) The piezopotential distribution of the $CaZr_{1-x}Cr_xO_3$ as applied compressive stress ($\sim 10^6$ MPa) that simulated under applying a hydrostatic pressure underwater.

(325 nm) was employed as an excitation source at room temperature to investigate the optical properties of the materials. A time-resolved-PL spectrometer (TRPL, Horiba Jobin Yvon, iHR550), based on a time-correlated single-photon counting method and equipped with a laser (405 nm) as an excitation source, was employed to characterize excited free-carrier dynamics with regard to the pumping intensity. Ultraviolet-visible spectrophotometry (UV–vis Hitachi, U3900) was used to measure the absorption of the samples and obtain absorption spectra. A ferro-electric analyzer (Keithley 4200) in the virtual ground mode was used to measure ferroelectric characteristics; the applied voltage was 5 V, and the hysteresis frequency was 100 Hz. The electrical properties of the metal oxides and doped samples were measured using a Hall measure-ment system (Ecopia, HMS-3000).

The 9–38 HEO samples were mixed with a methylene blue solution (10 ppm) to determine their dye degradation performance; $CaZrO_3$, $CaZrO_3$:Cr, $ZrYCeO_2$, and $ZrYCeCrO_2$ were used as control samples. An adsorption test was conducted by placing each sample in a dye solution in a dark environment for 30 min. Subsequently, dye degradation ex-periments were performed under light irradiation (with a 150-W Xe lamp), ultrasonic vibration (at 40 kHz and 250 W), and synthetic ul-trasonic vibration and light irradiation for investigating the

photocatalytic, piezocatalytic, and photopiezocatalytic activities, respectively. The best sample of 38HEO was used to evaluate HER performance by applying 1200 V, and unpolarized 38HEO was used as a control sample. The catalyst was dispersed in 5 mL methanol and 15 mL distilled water. The reactor was in a closed-loop associated with gas chromatography (GC1000TCD) and was conducted with a thermal conductivity detector to determine the gas composition [39].

2.3. Computational method

The piezopotential of the ferroelectric HEOs was calculated using the COMSOL Multiphysics simulation software. The theoretical calculations of this work were based on Density Functional Theory (DFT) [40] along with Vienna Ab initio Simulation Package (VASP) [41,42] software. The exchange-correlation functional was described by generalized gradient approximations (GGA) in Perdew–Burke–Ernzerhof (PBE) [43] func-tional, where projected augmented wave (PAW) [44] was given as pseudopotential. For all following calculations, the plane wave cutoff energy was set to 750 eV. The density of states (D.O.S.) calculations were performed with a Gamma-centered k-point mesh with a Monkhorst-Pack for $8 \times 8 \times 8$ [45].

A Ca$_4$Zr$_4$O$_{12}$ cell was used for the model of pristine CaZrO$_3$ calculation [46], while the CaZr$_{1-x}$Cr$_x$O$_3$ model was built by substituting one of the Zr atoms with a Cr atom, leading to the Zr: Cr ratio to be 3:1. A structural relaxation was conducted to ensure the interatomic forces were less than $0.02 eV/\mathring{A}$. A tightly converged electronic wavefunction of tolerance is $1 \times 10^{-7} eV$. After that, the local density of states (LDOS) was calculated, and after-processed with VASPKIT [47] density of states data processing functions. Furthermore, the density functional perturbation theory (DFPT) approach, implemented in the VASP was applied to predict the piezoelectric tensor of both CaZrO$_3$ and CaZr$_{1-x}$Cr$_x$O$_3$. COMSOL Multiphysics was used to simulate the piezoelectric potential of the CaZrO$_3$ and CaZr$_{0.95}$Cr$_{0.05}$O$_3$ nanoparticles. The piezoelectric tensor of CaZrO$_3$ and CaZr$_{0.95}$Cr$_{0.05}$O$_3$ were imported from the result of DFT. The porous fluorite structure of the ZrO$_2$-based compound embedded with the CaZrO$_3$ and CaZr$_{0.95}$Cr$_{0.05}$O$_3$ nanoparticles was constructed for our simulation model. The pressure was applied to the model, simulated from ultrasonic vibration to calculate the piezoelectric potential output. The generated pressure reached approximately 4.68×10^6 Pa under ultrasonic vibration (200 W) based on FEM calculations.

3. Results and discussion

3.1. Materials characterization of HEO and its ferroelectric property

We varied the Ca concentration in the (ZrYCeCr)O$_2$-based compound—using the values 9, 17, 29, 38, 44, and 50 at%—to cause precipitation of a ferroelectric phase, resulting in the HEOs termed 9HEO, 17HEO, 29HEO, 38HEO, and 50HEO, respectively. The calculated composition of all the samples and the corresponding results of inductively coupled plasma atomic emission spectrometry (ICP-AES) is given in Table S1 (Supporting Information). The scanning electron microscopy (SEM) image displayed in Fig. 1a shows that the HEOs were highly porous nanostructures. As shown by the X-ray diffraction (XRD) pattern presented in Fig. 1b, the HEOs were solid solutions comprising (CaZrYCeCr)O$_2$ and CaZrO$_3$ compounds. Upon increasing the proportion of Ca in the HEO to approximately 17 at% (17HEO), calcium zirconate (CaZrO$_3$, orthorhombic structure) with the space group *pnma* (JCPDS no. 35–0790) precipitated, as shown in Fig. 1b. Notably, the characteristic peaks at 2θ values of 46° and 48.5° in Fig. 1c—which can be attributed to CaZrO$_3$ and the (CaZrYCeCr)O$_2$ fluorite structure, respectively—shifted to a lower angle with increasing Ca concentration. The shift of the XRD pattern to a lower angle was attributed to the partial replacement of the Zr^{+4} ions by Cr^{+3} ions to form Ca(Zr$_{1-x}$Cr$_x$)O$_3$ because they have the same coordination number and similar atomic radii; such substitution caused a considerable compressive strain in the HEOs. The reason can also be attributed to the further substitution of Y^{+3} and Ce^{+4} with excess Ca ions to form a substitutional solid solution. Fig. 1d shows the transmission electron microscopy (TEM) energy-dispersive X-ray spectroscopy map of the elements Ca, Zr, Y, Ce, Cr, and O in the 9HEO. The five elements were uniformly distributed. Notably, Ca, Zr, Cr, O elements can be distinguished from Fig. 1d (marked by a circle), suggesting that the Ca(Zr$_{1-x}$Cr$_x$)O$_3$ has been formed (see detailed below). A low-magnitude TEM image of the HEO is shown in Fig. 1e. The corresponding high-resolution TEM (HRTEM) image, presented in Fig. 1f, the 38HEO and Ca(Zr$_{1-x}$Cr$_x$)O$_3$ crystals reveal phase boundaries with a considerable lattice mismatch. The HRTEM image of Ca(Zr$_x$Cr$_{1-x}$)O$_3$ displayed in Fig. 1g corresponds to the characteristic (112) plane of an orthorhombic crystal structure (space group *pnma*, 62), and the FFT patterns (inset of Fig. 1g) obtained along (112) correspond to lattice fringes of approximately 0.24 nm. Fig. 1h presents an HRTEM image of the 38HEO in which the lattice spacings of 0.30 nm and 0.27 nm are corresponding to the characteristic (111) and (200) planes of the fluorite structure, respectively, as shown in the inset of Fig. 1h.

Fig. 2a shows the polarization versus electric field curves for the various Ca concentrations. The ferroelectric polarization clearly yielded a hysteresis loop that enabled determination of the remanent polarization (P$_r$) and coercive field (E$_c$). Notably, the ferroelectric polarization of CaZr$_{1-x}$Cr$_x$O$_3$ increased with the HEO's Ca content and was highest when the Ca content was approximately 38 at% (38HEO). As the Ca concentration in the HEO was further increased, however, P$_r$ decreased, suggesting that the number of oxygen vacancies increased with an increase in the Ca concentration and that the ferroelectric polarization did not occur [48]. Therefore, electron paramagnetic resonance (EPR) was employed to investigate the concentration of oxygen vacancies in the HEO. As shown in Fig. 2b, the concentration of oxygen vacancies was strongly dependent on the Ca concentration in the HEO. For quantitative analysis, the concentration of oxygen vacancies and ferroelectric polarization as a function of the Ca concentration in the HEO were further divided into three stages (namely the first, second, and third stages), as illustrated in Fig. 2c. The oxygen vacancies increased with the Ca concentration in the first stage, namely in the cases 7HEO–19HEO. The slightly enhanced P$_r$ value was too small and, therefore, negligible. In the second stage, for 19HEO–38HEO, the P$_r$ value increased substantially and the oxygen concentration decreased upon an increase in the Ca content. In the third stage, for 38HEO–50HEO, P$_r$ decreased with an increase in the Ca content, suggesting more extensive precipitation of CaO, which led to an increase in the number of oxygen vacancies. P$_r$ was inversely proportional to the concentration of oxygen vacancies. Based on the material characterization and EPR analysis, we concluded that pristine CaZrO$_3$ does not have excellent ferroelectric properties. However, Ca(Zr$_{1-x}$Cr$_x$)O$_3$, which is ferroelectric, formed when the Ca content of the HEO was increased. As shown by the crystallographic structure in Fig. 2d, we postulated that during the annealing process, many trivalent Cr^{3+} ions were oxidized to form tetravalent Cr^{4+} ions, leading to the substantial annihilation of oxygen vacancies [49], and that Zr^{4+} ions were partially replaced by Cr^{4+} ions to yield Ca(Zr$_x$Cr$_{1-x}$)O$_3$. The Ca atom is surrounded by six oxygen atoms in the CaO$_6$ polyhedra. Further, the Cr^{4+} ions (diameter: 63 pm) substituted for the host Zr^{4+} ions (86 pm), where the Cr^{4+} ions resided in CrO$_6$ with nonequivalent positions, and the size difference between the two ions was approximately 23 pm (Fig. 2e). This ionic displacement caused spontaneous polarization due to the noncentrosymmetric structure, contributing to the material's ferroelectricity [50,51]. The butterfly loop of the CaZrO$_3$ and Ca(Zr$_x$Cr$_{1-x}$)O$_3$ (i.e., x = 0.05) has been shown in Supplementary Information of Fig. S1a and S1b, respectively. The Ca(Zr$_x$Cr$_{1-x}$)O$_3$ exhibited a significant hysteresis loop compared with CaZrO$_3$.

Density functional theory (DFT) was used to calculate the piezoelectric constants of the CaZrO$_3$ and the Ca(Zr$_x$Cr$_{1-x}$)O$_3$. To simplify, the Zr:Cr ratio was chosen 3:1 for calculation because the simulation for a small amount of Cr doping ratio needs to create a large supercell, leading to a highly lengthy calculation time. The configuration of Ca(Zr$_x$Cr$_{1-x}$)O$_3$ is shown in Fig. 2f. Fig. 2g revealed Cr occupying substitutional site #1 and #3. The results revealed that Cr occupied sites 1 and 3 could obtain the lowest free energy. For comparison, the piezoelectric constants (e$_{ij}$, C/m^2) of the CaZrO$_3$ and Ca(Zr$_x$Cr$_{1-x}$)O$_3$ are shown in Eq. (1) and Eq. (2), respectively. The piezoelectric constants derived for the CaZrO$_3$ are too small and were negligible compared with the Ca(Zr$_x$Cr$_{1-x}$)O$_3$. The Ca(Zr$_x$Cr$_{1-x}$)O$_3$ was applied by a 1 MPa (ultrasonic force) to simulate a catalyst placed under hydrostatic pressure by a water-filled ultrasonic container. The theoretical calculation based on the finite element method (FEM) revealed that the piezopotential was considerably increased on the edge sites, indicating the high ferroelectricity of Ca(Zr$_x$Cr$_{1-x}$)O$_3$ when compared with pristine CaZrO$_3$, as shown in Fig. 2h. Noted that the Ca(Zr$_x$Cr$_{1-x}$)O$_3$ exhibited shear stress-induced piezoelectric polarization, the piezopotential distribution did not align with the z-axis.

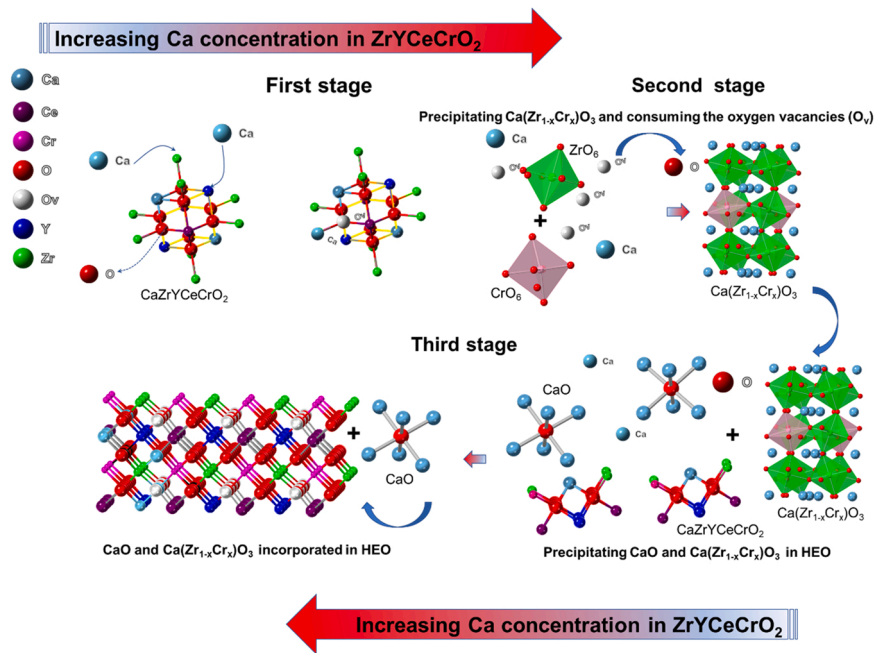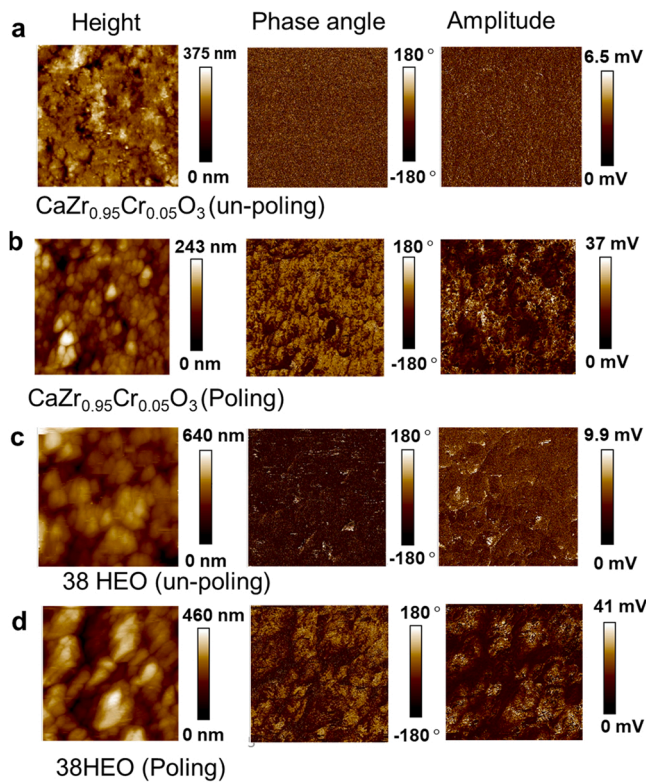**Fig. 3.** The formation process of the ferroelectric HEO that precipitated $CaZr_{1-x}Cr_xO_3$.

Fig. 4. The 3D image of the height sensor, the phase angle of the $CaZr_{0.95}Cr_{0.05}O_3$ and HEO for (a) before and (b) after applying electric polarization ~600 V. The height sensor and phase angle of the 38HEO for (c) before and (d) after applying electric polarization ~600 V.

$$e_{ij} = \begin{pmatrix} 0.06669 & -0.03641 & -0.01984 & 0.03935 & -0.00594 & -0.09444 \\ -0.06283 & -0.02461 & 0.04085 & 0.00274 & 0.06948 & 0.05065 \\ 0.01691 & 0.00763 & -0.01772 & 0.00357 & -0.01622 & -0.01692 \end{pmatrix}$$

$$(1)$$

$$e_{ij} = \begin{pmatrix} 0.0006 & -0.00006 & -0.00004 & 0 & 0 & 0 \\ -0.00017 & -0.00002 & 0.00005 & 0 & 0 & 0 \\ 0.00001 & 0.00003 & -0.00003 & 0 & 0 & 0 \end{pmatrix}$$

$$(2)$$

The formation process of the ferroelectric HEO is illustrated in Fig. 3. In the first stage, the Ca^{2+} ions combined with the fluorite $ZrYCeCrO_2$ progressively to form $Ca_xZrYCeCrO_2$ ($x = 0.09–0.17$), which led to an increase in the concentration of oxygen vacancies. This was because when the concentration of Ca^{2+} ions in the HEO was increased, the Ca^{2+} ions (0.112 nm) substituted for the Ce^{4+} (0.097 nm) and Y^{3+} (0.102 nm) ions, creating oxygen vacancies, as expressed in Eqs. (3) and (4):

$$CaO + 2Y_Y^x \rightarrow 2Ca_Y^{'} + 2V_o^{\bullet} + O_o$$

$$(3)$$

$$CaO + 2Ce_{Ce}^x \rightarrow 2Ca_{Ce}^{'} + V_o^{\bullet\bullet} + O_o$$

$$(4)$$

The creation of excessive oxygen vacancies likely caused further precipitation of $Ca(Zr_{1-x}Cr_x)O_3$ [52]. Therefore, the highest P_r value was observed in the second stage, for an intermediate Ca content, demonstrating that Ca ions combined with Cr^{3+} and Zr^{4+} to precipitate $Ca(Zr_{1-x}Cr_x)O_3$ along the grain boundaries, causing ferroelectric properties and reducing the number of oxygen vacancies. In the third stage, the increase in the concentration of oxygen vacancies was primarily because CaO was further precipitated in the HEO, leading to poorer ferroelectric properties of $Ca(Zr_{1-x}Cr_x)O_3$ because of the increase in the number of oxygen vacancies.

Piezoresponse force microscopy (PFM) was employed to investigate the ferroelectric properties of $Ca(Zr_{0.95}Cr_{0.05})O_3$ and 38HEO under the application of an electric field, (referred to as $Ca(Zr_{0.95}Cr_{0.05})O_3$-P and 38HEO-P). Fig. 4a and 4b reveal the topography and phase angle of polarized and unpolarized $Ca(Zr_{0.95}Cr_{0.05})O_3$ films. Based on the obtained phase amplitude and piezoresponse, the polarized $Ca(Zr_{0.95}Cr_{0.05})O_3$ had an apparent phase angle and piezoresponse amplitude, whereas the unpolarized one did not. Figs. 4c and 4d show the topography and phase angle of polarized and unpolarized 38HEO films. Under an applied electric field, the polarized 38HEO film exhibited
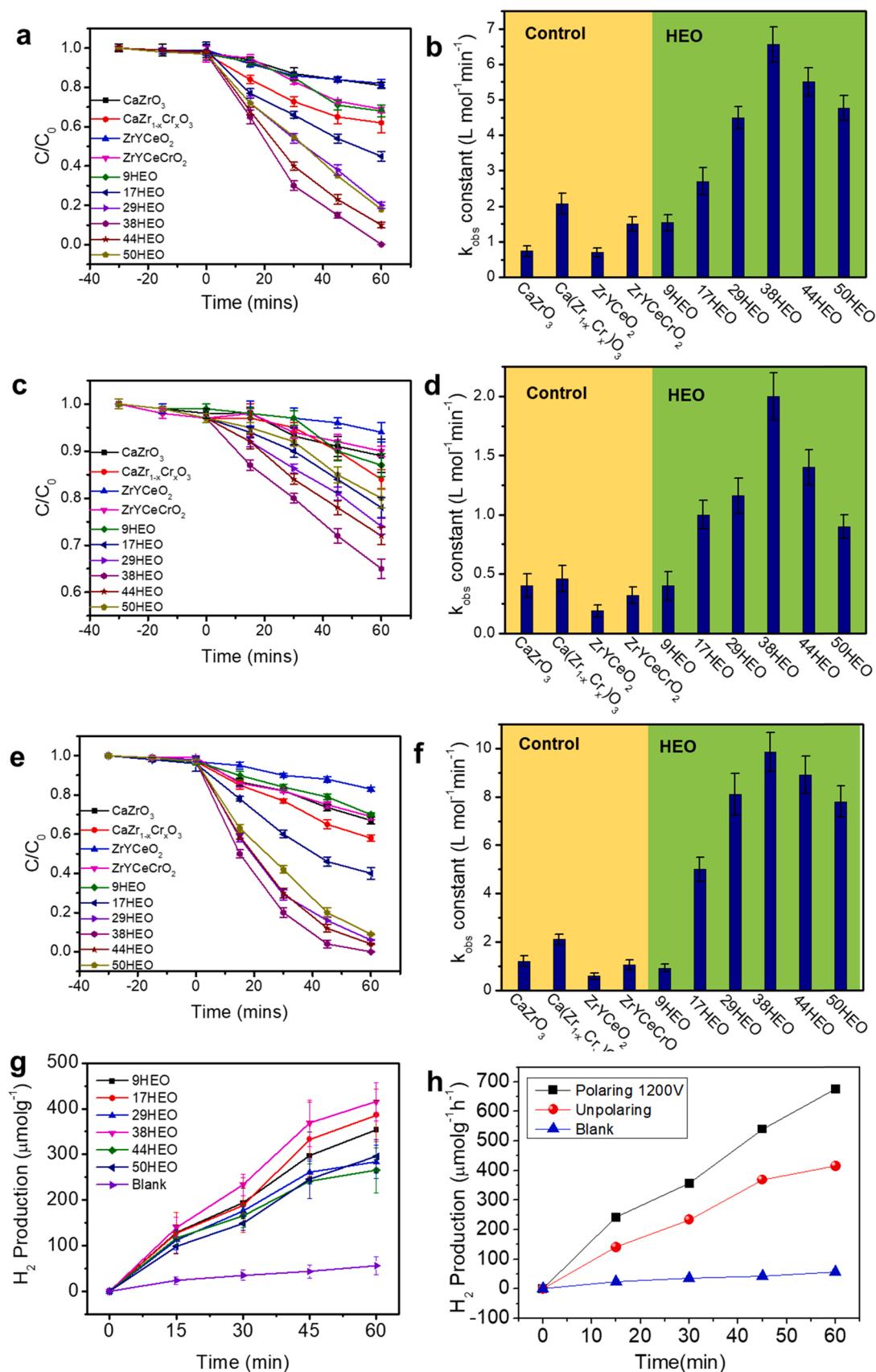
Fig. 5. The degradation performance of CaZrO$_3$, CaZr$_x$Cr$_{1-x}$O$_3$ (x = 0.05), ZrYCeO$_2$, ZrYCeCrO$_2$, 9–50HEO under (a) the photocatalytic process, (b) the corresponding reaction constant k$_{obs}$, (c) piezocatalytic process, (d) the corresponding reaction constant k$_{obs}$, (e) the piezo-photocatalytic process, (f) the corresponding reaction constant k$_{obs}$. (g) The H$_2$ production performance of the 9–50HEO under the piezo-photocatalytic process. (h) Comparing the H$_2$ production performance of the 38HEO before and after applying 1200 V.
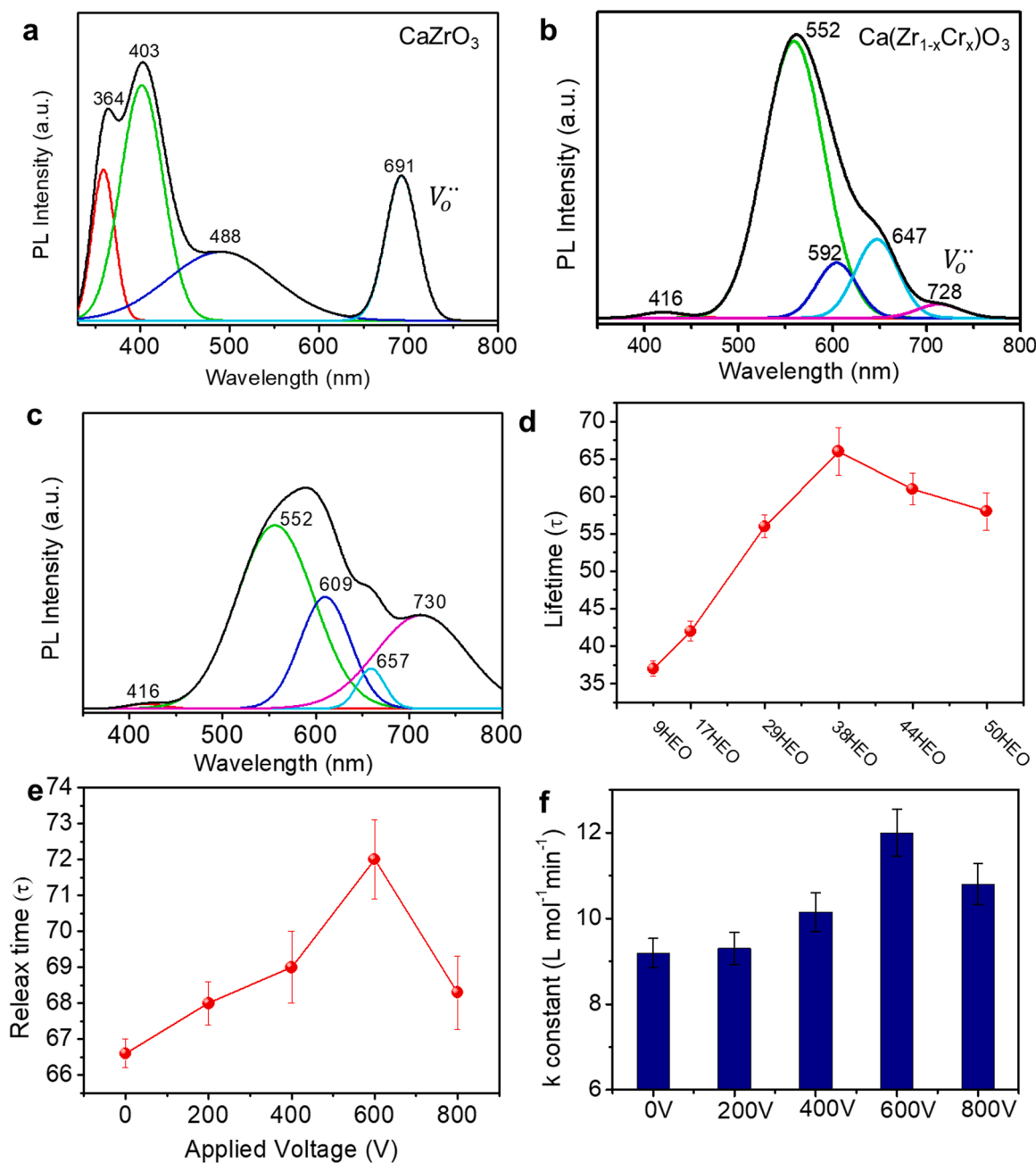
Fig. 6. The photoluminescence spectra of the (a) CaZrO$_3$, (b)CaZr$_x$Cr$_{1-x}$O$_3$ ($x = 0.05$), (c) 38HEO, (d) the carrier's lifetime as a function of Ca concentration of HEO. (e) the carrier's lifetime of the 38HEO as a function of applied voltage. (f) The corresponding reaction constant (k_{obs}) of dye degradation as a function of the applied electric field of the 38HEO.

greater phase amplitude and piezopotential output than did the unpolarized 38HEO film. The high piezopotential output of the polarized 38HEO film suggests that Cr^{3+} ions partially substituted for host Zr^{3+} ions, causing a substantial piezopotential output under severe distortion of the HEO lattice. The results showed that the piezoelectric response was greater in both polarized Ca(Zr$_{0.95}$Cr$_{0.05}$)O$_3$ and 38HEO than in the equivalent unpolarized compound. Furthermore, the Ca(Zr$_{0.95}$Cr$_{0.05}$)O$_3$ was uniformly dispersed in 38HEO. Consequently, we concluded that the HEO catalyst could be optimized efficiently to achieve the piezopotential effect by increasing the Ca content and affecting the number of oxygen vacancies in the HEO through precipitation of the ferroelectric Ca(Zr$_{0.95}$Cr$_{0.05}$)O$_3$. The results also revealed the existence of a preferred polarization direction—outward from the crystal plane of the ferroelectric Ca(Zr$_{0.95}$Cr$_{0.05}$)O$_3$—which was found to play a crucial role in the

HEO compound when an external bias was applied.

3.2. Piezodegradation and hydrogen evolution activity of ferroelectric HEOs

HEOs with various Ca concentrations (9HEO–50HEO) and control samples of CaZrO$_3$, Ca(Zr$_{0.95}$Cr$_{0.05}$)O$_3$, (Zr$_{0.33}$Y$_{0.33}$Ce$_{0.33}$)O$_2$, and (Zr$_{0.3}$Y$_{0.3}$Ce$_{0.3}$Cr$_{0.1}$)O$_2$ were prepared (see the XRD patterns in Supplementary Information of Fig. S2), and their catalytic activity toward the decomposition of an organic dye, namely methylene blue, through photocatalytic, piezocatalytic, and piezo–photocatalytic processes was investigated. Fig. 5a and 5b indicate that the photocatalytic degradation activities of Ca(Zr$_{0.95}$Cr$_{0.05}$)O$_3$ and 38HEO were superior to those of the pristine CaZrO$_3$, (Zr$_{0.33}$Y$_{0.33}$Ce$_{0.33}$)O$_2$, and (Zr$_{0.3}$Y$_{0.3}$Ce$_{0.3}$Cr$_{0.1}$)O$_2$.

Notably, increasing the Ca concentration in the HEO up to 38 at% progressively increased the degradation efficiency; specifically, 38HEO exhibited excellent performance, with the highest k_{obs} of approximately 6.56 L mol^{-1} min^{-1}. An evaluation of the piezocatalytic process revealed that the degradation activity of Ca(Zr$_{0.95}$Cr$_{0.05}$)O$_3$ was greater than that of pristine CaZrO$_3$, as illustrated in Figs. 5c and 5d. Although its piezocatalytic degradation activity was lower than its photocatalytic activity, 38HEO exhibited the highest degradation activity among all the samples (including control and HEO samples), indicating that increasing the Ca concentration optimized the piezopotential in the HEO, thereby enhancing the piezocatalytic activity. The piezodegradation activity finding is consistent with our PFM results, according to which the precipitation of ferroelectric Ca(Zr$_{1-x}$Cr$_x$)O$_3$ in HEO compounds plays a vital role, resulting in the excellent degradation activity of 38HEO. Regarding photo–piezocatalytic activity, Figs. 5e and 5f indicate that 38HEO had the highest dye decomposition ratio, approximately 99%; this value is 1.5 and 4.9 times higher than that of the same catalyst in the photocatalytic and piezocatalytic processes, respectively. In addition, the photo–piezocatalytic activity of 38HEO was nearly 5 times that of the control samples and 9HEO. The HEO samples with various Ca concentrations were further investigated in terms of their hydrogen evolution reaction (HER) activity in the synthetic piezo–photocatalytic process (Fig. 5g). Consistently, the hydrogen production was found to be highest for 38HEO at approximately 415 μmolg^{-1} h^{-1}. In addition, application of an external bias of 1200 V further improved the hydrogen production of 38HEO to 677 μmolg^{-1} h^{-1}, 163% that of the unpolarized 38HEO (Fig. 5h), demonstrating that a spontaneous electric polarization can be reversed by an externally applied electric field, which is consistent with our PFM and P-E curves results. Based on these results, 38HEO had excellent piezodegradation and hydrogen production performance, implying that 38HEO had deep trapping states and ferroelectric polarization, which played a crucial role in its high catalytic activity through the photo- and piezo-induced charge separation processes.

Photoluminescence (PL) was used to investigate the trapping states of the HEO. The PL spectrum of Fig. 6a reveals that the spectrum of CaZrO$_3$ had four peaks. The blue emission at 364 and 403 nm was attributed to structural imperfections in the energy levels of the complex clusters of [CaO$_7$·Vo]-[CaO$_7$·Vo] in the CaZrO$_3$ [53–55]. The 488 and 691 nm peaks confirmed deep-level defect emissions from ZrO$_6$ clusters and oxygen vacancies, respectively. The PL spectrum of Ca(Zr$_{0.95}$Cr$_{0.05}$)O$_3$, presented in Fig. 6b, indicates that Cr^{3+} was oxidized into Cr^{4+}, causing substitution of the host atom Zr^{4+} with Cr^{4+} through consumption of the oxygen vacancies. Therefore, the oxygen vacancy concentration in Ca(Zr$_{1-x}$Cr$_x$)O$_3$ was lower than that in pristine CaZrO$_3$, exhibiting superior piezocatalytic activity. The PL spectrum of Ca(Zr$_{0.95}$Cr$_{0.05}$)O$_3$ reveals that the Cr^{4+} dopant lowered the bandgap and suppressed the near-band emission of Ca-complex clusters [56]. In this context, the change in position of the prominent peak from 364 to 552 nm was attributed to transfer of the emission peak from shallow defects (CaO$_6$) to deep defects (ZrO$_6$). We observed that the Cr^{4+} dopants effectively narrowed the bandgap by approximately 1.1 eV owing to the Cr 3d orbital introducing a new band, within the origin bandgap, that served as a charge-transfer band between hybrid 3d orbitals (i.e., Zr and Cr 3d) [57]. The prominent peak in the spectrum of 38HEO at approximately 416 nm, shown in Fig. 6c, was ascribed to Ca^{2+} clusters (2.98 eV, located in the ultraviolet region). The peaks at 552 and 609 nm correspond to the emission states (Zr^{4+} and Cr^{3+}); the peaks at 557 nm and 730 nm were assigned to deep-level emission (i.e., oxygen vacancies). Therefore, the HEO had multiple electron-trapping states and oxygen vacancies in its band structure and exhibited emissions corresponding to the ferroelectric second phase.

In semiconductor materials, dopants and defects generally create the intermediate energy levels that serve as deep traps for electrons and holes or as recombination centers that enhance photocatalytic activity [58]. We determined how such defect centers, when coupled with piezoelectric polarization in an HEO, can influence the lifetime of carriers. Fig. 6d reveals that 38HEO exhibited the longest carrier lifetime among all the samples. We varied the voltage from 200 to 800 V to polarize the 38HEO samples and observed the dye degradation reaction constant for each polarized sample. Fig. 6e shows that the optimal carrier lifetime was attained at 600 V for the 38HEO. This result was consistent with that of the rate constant (k_{obs}) for the degradation of the dye molecules (Fig. 6f). An increase in polarization further separated the electron-hole pairs, driving them in opposite directions and increasing the likelihood of radiative relaxation. The results obtained for the polarized HEO sample indicated that ferroelectric polarization further prolonged the lifetime of radiative and nonradiative processes by enabling charge separation. In addition, the 38HEO sample polarized under an applied bias of 600 V had a carrier lifetime 1.3 times that of the unpolarized samples, indicating that the external bias promoted charge separation and enhanced the activity of the catalyst. The rate constant (k_{obs}) for applying a bias of 800 V exhibited a lower degradation activity than that for 600 V. The reason was that the highly applied bias was breakdown due to the porosity of the HEO compound. The 38HEO has been evaluated their stability after the HER process, as shown in Fig. S3 (XRD pattern, Supplementary Information).

The variation of Ca content played a crucial role in modulating the concentration of oxygen vacancies and the generation of ferroelectricity in the HEO. On the basis of Hall measurements, the ferroelectric Ca(Cr$_{1-x}$Zr$_x$)O$_3$ was determined to be a p-type semiconductor with a carrier concentration of 3.436×10^{12} cm^{-3}, whereas the fluorite CaZrY-CeCrO$_2$ was found to be an n-type semiconductor with a carrier concentration of -1.92×10^{12} cm^{-3}.[59] For simplicity, a Ca(Cr$_{1-x}$Zr$_x$)O$_3$/HEO heterostructure was constructed to explain piezopotential-catalyzed dye degradation and hydrogen evolution activity in terms of the distribution of acceptors (N_A) and donors (N_D) in the junction region. The change in built-in potential (ψ_{bi}) as a result of piezoelectric charges (W_{piezo}) arising from compressive and tensile strain is expressed in Eq. (5), which defines the sign of the local piezoelectric charges.[60].

$$\psi_{bi} = \frac{q}{2\varepsilon_s}\left(N_A W_{Dp}^2 + N_D W_{Dn}^2 + \rho_{piezo(x)} W_{piezo}^2\right) \quad (5)$$

where $N_{D(x)}$ is the donor concentration, $N_{A(x)}$ is the acceptor concentration, $\rho_{piezo(x)}$ is the density of the piezoelectric charge, ε_s is the permittivity of the piezoelectric material, and W_{piezo} is the width of the piezoelectric charges distributed at the p–n junction interface, which is related to the Fermi level (E_F) in the presence of a piezopotential, given by Eq. (6).

$$E_F = E_{F0} - \frac{q^2 \rho_{piezo(x)} W_{piezo}^2}{2\varepsilon_s} \quad (6)$$

Eq. (6) implies that piezoelectric charges can modulate Fermi levels and that the piezoelectric charges are proportional to the charge transported across the p–n junction, which is an exponential function of the local piezoelectric charge, the sign of which is dependent on the strain, as given by Eq. (7).

$$J \propto \exp\left(\frac{q^2 \rho_{piezo(x)} W_{piezo}^2}{2\varepsilon_s kT}\right) \quad (7)$$

In addition, the density of the piezoelectric charge is proportional to the piezopotential (P), as given in Eq. (8). This demonstrates that the piezopotential can modulate the semiconductor energy band relative to the Fermi level.

$$P = e_{ijk} s_{jk} = q \rho_{piezo(x)} W_{piezo} \quad (8)$$

where the third-order tensor (e_{ijk}) is the piezoelectric tensor and s_{jk} is the strain related to the piezoelectric polarization. Therefore, the induced piezocharge (or piezoelectric polarization) contributes to the built-in potential and electric field (E) to separate electron-hole pairs [18,61,
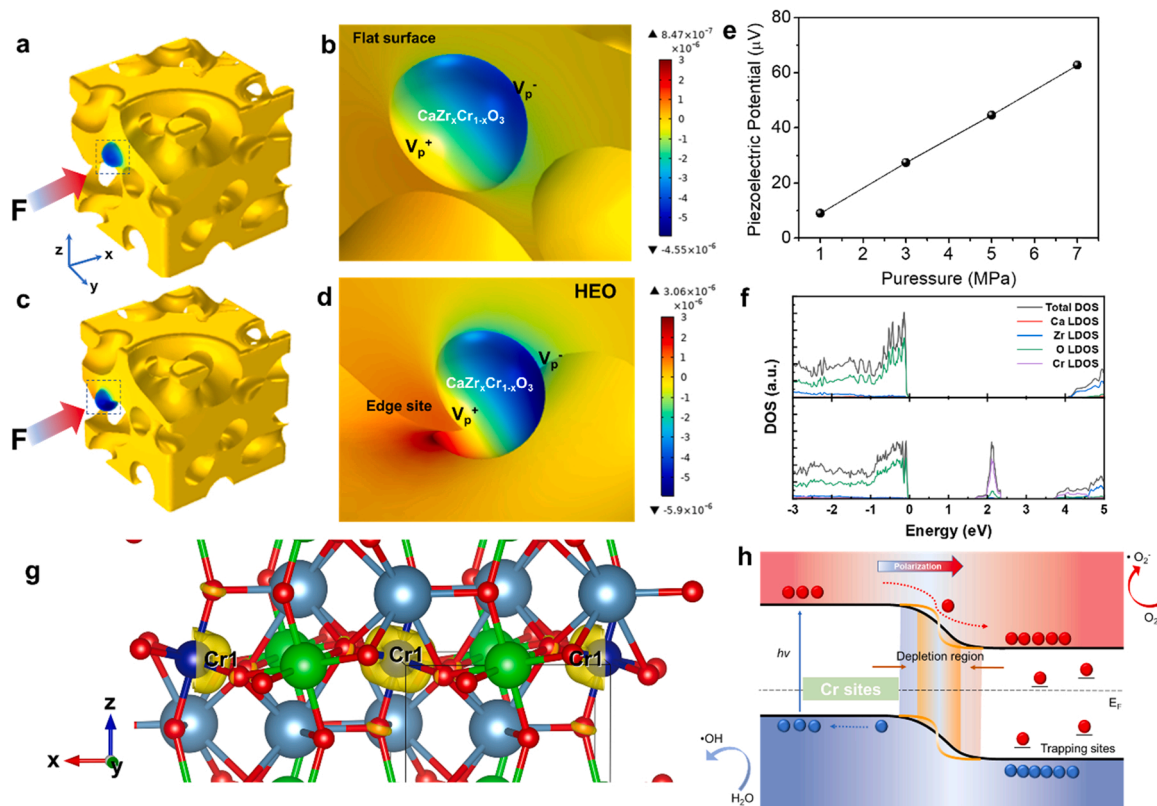
Fig. 7. The piezopotential distribution of a CaZr$_{1-x}$Cr$_x$O$_3$ nanoparticle implanted on the (a)-(b) flat surface of the porous HEO, (c)-(d) the edge site of the porous HEO. (e) The plot of the piezopotential difference of ferroelectric HEO as a function of the applied pressure along with *x*-direction. (f) The local density of states (LDOS) of pristine CaZrO$_3$ (upper image) and CaZr$_{0.75}$Cr$_{0.25}$O$_3$ (lower image), where substituting Zr with Cr in the CaZrO$_3$ with the ratio of Zr:Cr= 3:1. (g) The decomposed charge density of CaZr$_{0.75}$Cr$_{0.25}$O$_3$ formed an impurity state localized at the Cr site. (h) The charge transfer mechanism of the CaZr$_{1-x}$Cr$_x$O$_3$/HEO indicates that the piezoelectric polarization can modulate the depletion zone of the heterojunction, enhancing the electrochemical redox process of ferroelectric HEO.

62].

3.3. Charge-transfer mechanism in ferroelectric HEOs

The charge-separation mechanism of the ferroelectric HEOs is further depicted in Fig. 7. Nanoparticles of the ferroelectric Ca(Zr$_{1-x}$Cr$_x$)O$_3$ were implanted into the HEO (flat surface), which was then subjected to compressive stress along the *x*-axis. The consequent piezoelectric polarization is shown in Figs. 7a and 7b. The computational results displayed in Figs. 7c and 7d demonstrate that when the ferroelectric Ca(Zr$_{1-x}$Cr$_x$)O$_3$ was implanted at the edge sites of the porous HEO, the piezopotential output was approximately 3.6 times of magnitude greater than that when Ca(Zr$_{1-x}$Cr$_x$)O$_3$ was implanted at the flat surface of HEO (Figs. 7a and 7b). The piezopotential of the ferroelectric HEO was proportional to the applied mechanical force (Fig. 7e). The FEM theoretical calculation result shows that because of the localized strain in the interfacial area, the piezopotential of the ferroelectric Ca(Zr$_{1-x}$Cr$_x$)O$_3$ was strongly coupled with the charge transfer on the HEO's surface. The DFT calculated result shows that the local density of states (LDOS) of pristine CaZrO$_3$ is given in Fig. 7f (upper image), and a large band gap (~4 eV) shows an insulated electrical property of pristine CaZrO$_3$. After substituting Zr with Cr in CaZrO$_3$ with the ratio of Zr:Cr= 3:1, a gap state (~+2 eV) formed at valence band maximum (VBM), indicating that the formation of the impurity state caused by Cr doping that localized at Zr sites (Fig. 7f, lower image). Notably, the 0 eV point of the energy axis is aligned to the VBM in both figures. Based on the LDOS, the impurity states were mainly contributed by Cr dopants, confirmed by the decomposed charge density of CaZr$_{0.75}$Cr$_{0.25}$O$_3$, as shown in Fig. 7g. The spatial dispersion of the band forms the impurity states. The yellow isosurface is distributed only near the doped Cr atom, evidencing that

the band forms an impurity state localized at the Cr site. The DFT calculation was consistent with our PL spectrum of the CaZr$_{1-x}$Cr$_x$O$_3$ that a Cr impurity state was observed at 552 nm (Fig. 6b).

Therefore, Fig. 7h shows that the piezopotential of the Ca(Zr$_{1-x}$Cr$_x$)O$_3$ can modulate the built-in potential of the heterojunction, thereby tuning the depletion zone at the Ca(Zr$_{1-x}$Cr$_x$)O$_3$/HEO interfacial area. Besides, the PL spectra indicate that the intrinsic emission of the HEO was located at 418 nm, with strong emission bands also found at 552, 609, 657, and 730 nm, which were respectively attributed to Zn^{+4}, Cr^{3+}, and oxygen vacancies (V$_o^{\bullet}$ and V$_o^{\bullet\bullet}$) that contributed to the defect levels in the band structure, effectively acted as carriers separation center. Fig. 7h further shows that the depletion zone became smaller with an increase in the built-in potential owing to the piezoelectric polarization of ferroelectric HEO and further enhanced the charge transfer in the junction area. The band structure of semiconductors and redox potentials of water splitting for the 38HEO and CaZr$_{1-x}$Cr$_x$O$_3$ are shown in Fig. S4 (Supplementary Information). Thus, the simulation results revealed how the high piezopotential of the ferroelectric Ca(Zr$_{1-x}$Cr$_x$)O$_3$ coupled with the HEO, thereby modulating the charge carriers to achieve separation in the interfacial area. In this study, the ferroelectric Ca(Zr$_{1-x}$Cr$_x$)O$_3$ was implanted in a porous HEO matrix, which offers numerous edge sites to produce a considerable piezopotential localized in the interfacial area. The aforementioned piezopotential enhanced the electric field at the heterojunction and gave the ferroelectric HEO nanocomposite excellent catalytic performance.

4. Conclusion

This study fabricated HEO catalysts comprising ferroelectric Ca(Zr$_{1-x}$Cr$_x$)O$_3$ and CaZrYCeO$_2$. A noncentrosymmetric structure with the

Table 1
The piezoelectric constant of the $CaZrO_3$.

e_{ij} (C/m^2)	XX	YY	ZZ	YZ	ZX	XY
X	-0.0128	-0.01134	0.03663	0	0.05097	0
Y	-0.00653	-0.01916	0.02221	0	0.03191	0
Z	-0.00168	0.01157	-0.00912	0	-0.00856	0

Table 2
The piezoelectric constant of the $CaZrO_3$:Cr.

e_{ij} (C/m^2)	XX	YY	ZZ	YZ	ZX	XY
X	0.00006	0.00004	0.00008	0	0	0
Y	0.00017	0.00002	0.00005	0	0	0
Z	-0.00001	-0.00003	0.00003	0	0	0

space group *pnma*, namely $Ca(Zr_{1-x}Cr_x)O_3$ (x = 0.05), was precipitated in the HEO by modulating the Ca concentration. The ferroelectric Ca $(Zr_{0.95}Cr_{0.05})O_3$ acted as an efficient separator of electron-hole pairs, and when coupled with defect sites, provided trapping centers in the piezocatalytic process, substantially prolonging the carrier lifetime to approximately 66 ns. Through a synergistic piezophototronic application, the 38HEO catalyst had excellent dye decomposition efficiency, approximately 800% higher than that of its pristine counterpart. The Ca concentration of the HEO strongly affected the formation of oxygen vacancies. The remnant polarization of the ferroelectric HEO was inversely proportional to the concentration of oxygen vacancies. Notably, the reaction rate constant of 38HEO for the decomposition of dye molecules was 1000% that of pristine $ZrYCeCrO_2$. The ferroelectric HEO exhibited deep levels such as those corresponding to complex clusters with visible-light absorbance and multiple electron-trapping states such as Zr^{+4}, Y^{+3}, Ce^{+4}, Cr^{3+}, and oxygen vacancies; these, when coupled with the piezopotential of the ferroelectric HEO, led to a prolonged carrier lifetime owing to the enhancement of radiative processes by charge separation. This in turn enhanced the photocatalytic activity of the HEO. The polarized 38HEO achieved hydrogen production of 677 $\mu molg^{-1}$ h^{-1}, 163% that of the unpolarized 38HEO. Simulation results indicated that the width of the depletion zone could be tuned by modulating the mechanical force on the ferroelectric Ca $(Zr_{1-x}Cr_x)O_3$, thereby promoting electron-hole pair separation. A ferroelectric second phase with abundant trapping states at deep levels could be precipitated in the ferroelectric HEO, increasing the probability of electron transitions in trapping states and enhancing the photocatalytic performance. The concepts newly developed in this study can be employed to fabricate next-generation piezocatalysts.(Tables 1 and 2).

CRediT authorship contribution statement

J.M.W.: conceptualization, investigations, writing, and supervision. **S. C. C., H.-Y.C., P. H. C., J. T. L.**: experiments, investigations, data curation, theoretical calculation, and draft writing. **S. C. C.** and **H.-Y.C.** contributed equally. All authors have approved the final version of the manuscript.

Declaration of Competing Interest

The authors declare that they have no known competing financial interests or personal relationships that could have appeared to influence the work reported in this paper.

Data Availability

Data will be made available on request.

Supplementary information

regarding the piezoelectric tensor calculated by DFT, XRD, detailed composition of all the HEO samples, is attached to this paper.

Appendix A. Supporting information

Supplementary data associated with this article can be found in the online version at doi:10.1016/j.apcatb.2022.122204.

References

[1] T. Takata, J.Z. Jiang, Y. Sakata, M. Nakabayashi, N. Shibata, V. Nandal, K. Seki, T. Hisatomi, K. Domen, Photocatalytic water splitting with a quantum efficiency of almost unity, Nature 581 (2020) 411 (+).

[2] K. Maeda, K. Teramura, D.L. Lu, T. Takata, N. Saito, Y. Inoue, K. Domen, Photocatalyst releasing hydrogen from water - Enhancing catalytic performance holds promise for hydrogen production by water splitting in sunlight, Nature 440 (2006), 295-295.

[3] Y.W. Gao, Y. Wang, H. Zhang, Removal of Rhodamine B with Fe-supported bentonite as heterogeneous photo-Fenton catalyst under visible irradiation, Appl. Catal. B Environ. 178 (2015) 29–36.

[4] H. Fei, J.X. Shao, H. Li, N.J. Li, D.Y. Chen, Q.F. Xu, J.H. He, J.M. Lu, Construction of ultra-thin 2D CN-Br-0.12/2%RhOx photo-catalyst with rapid electron and hole separation for efficient bisphenol A degradation, Appl. Catal. B Environ. 299 (2021).

[5] L.Q. Deng, K. Zhang, D. Shi, S.F. Liu, D.Q. Xu, Y.L. Shao, J.X. Shen, Y.Z. Wu, X. P. Hao, Rational design of Schottky heterojunction with modulating surface electron density for high-performance overall water splitting, Appl. Catal. B Environ. 299 (2021).

[6] J.M. Wu, Y.R. Chen, W.T. Kao, Ultrafine ZnO nanoparticles/nanowires synthesized on a flexible and transparent substrate: formation, water molecules, and surface defect effects, ACS Appl. Mater. Inter 6 (2014) 487–494.

[7] Z.H. Xue, D.Y. Luan, H.B. Zhang, X.W. Lou, Single-atom catalysts for photocatalytic energy conversion, Joule 6 (2022) 92–133.

[8] Y. Chen, Y.M. Zhang, G.Z. Fan, L.Z. Song, G. Jia, H.T. Huang, S.X. Ouyang, J.H. Ye, Z.S. Li, Z.G. Zou, Cooperative catalysis coupling photo-/photothermal effect to drive Sabatier reaction with unprecedented conversion and selectivity, Joule 5 (2021) 3235–3251.

[9] M. Reli, N. Ambrozova, M. Sihor, L. Matejova, L. Capek, L. Obalova, Z. Matej, A. Kotarba, K. Koci, Novel cerium doped titania catalysts for photocatalytic decomposition of ammonia, Appl. Catal. B Environ. 178 (2015) 108–116.

[10] Y.H. Lin, P.S. Lee, Y.C. Hsueh, K.Y. Pan, C.C. Kei, M.H. Chan, J.M. Wu, T.P. Perng, H.C. Shih, Atomic layer deposition of zinc oxide on multiwalled carbon nanotubes for UV photodetector applications, J. Electrochem Soc. 158 (2011). K24-K27.

[11] M.C. Lin, S.N. Lai, K.T. Le, J.M. Wu, Self-powered photoelectrochemical quartz/ TiO2 microsystem through piezopotential sensitized photocatalytic process, Nano Energy 91 (2022).

[12] Z.L. Wang, J.H. Song, Piezoelectric nanogenerators based on zinc oxide nanowire arrays, Science 312 (2006) 242–246.

[13] J. Wu, X. Li, W. Shi, P. Ling, Y. Sun, X. Jiao, S. Gao, L. Liang, J. Xu, W. Yan, C. Wang, Y. Xie, Efficient visible-light-driven CO(2) reduction mediated by defect-engineered BiOBr atomic layers, Angew. Chem. Int Ed. Engl. 57 (2018) 8719–8723.

[14] W. Wu, L. Wang, Y. Li, F. Zhang, L. Lin, S. Niu, D. Chenet, X. Zhang, Y. Hao, T. F. Heinz, J. Hone, Z.L. Wang, Piezoelectricity of single-atomic-layer MoS2 for energy conversion and piezotronics, Nature 514 (2014) 470–474.

[15] Y. Zi, L. Lin, J. Wang, S. Wang, J. Chen, X. Fan, P.K. Yang, F. Yi, Z.L. Wang, Triboelectric-pyroelectric-piezoelectric hybrid cell for high-efficiency energy-harvesting and self-powered sensing, Adv. Mater. 27 (2015) 2340–2347.

[16] R. Su, Z.P. Wang, L.N. Zhu, Y. Pan, D.W. Zhang, H. Wen, Z.D. Luo, L.L. Li, F.T. Li, M. Wu, L.Q. He, P. Sharma, J. Seidel, Strain-engineered nano-ferroelectrics for high-efficiency piezocatalytic overall water splitting, Angew. Chem. Int Ed. 60 (2021) 16019–16026.

[17] Y. Zhang, P.T.T. Phuong, E. Roake, H. Khanbareh, Y.Q. Wang, S. Dunn, C. Bowen, Thermal energy harvesting using pyroelectric-electrochemical coupling in ferroelectric materials, Joule 4 (2020) 301–309.

[18] Y.W. Feng, M.J. Xu, H. Liu, W. Li, H.X. Li, Z.F. Bian, Charge separation and interfacial selectivity induced by synergistic effect of ferroelectricity and piezoelectricity on PbTiO3 monocrystalline nanoplates, Nano Energy 73 (2020).

[19] W.Z. Wu, L. Wang, Y.L. Li, F. Zhang, L. Lin, S.M. Niu, D. Chenet, X. Zhang, Y. F. Hao, T.F. Heinz, J. Hone, Z.L. Wang, Piezoelectricity of single-atomic-layer MoS2 for energy conversion and piezotronics, Nature 514 (2014) 470 (+).

[20] M.H. Wu, J.T. Lee, Y.J. Chung, M. Srinivaas, J.M. Wu, Ultrahigh efficient degradation activity of single- and few-layered MoSe2 nanoflowers in dark by piezo-catalyst effect, Nano Energy 40 (2017) 369–375.

[21] S. Masimukku, Y.-C. Hu, Z.-H. Lin, S.-W. Chan, T.-M. Chou, J.M. Wu, High efficient degradation of dye molecules by PDMS embedded abundant single-layer tungsten disulfide and their antibacterial performance, Nano Energy (2018).

[22] J.M. Wu, W.E. Chang, Y.T. Chang, C.-K. Chang, Piezo-catalytic effect on the enhancement of the ultra-high degradation activity in the dark by single- and few-layers MoS2 nanoflowers, Adv. Mater. 28 (2016) 3718–3725.

[23] J.-H. Lin, Y.-H. Tsao, M.-H. Wu, T.-M. Chou, Z.-H. Lin, J.M. Wu, Single- and few-layers MoS2 nanocomposite as piezo-catalyst in dark and self-powered active sensor, Nano Energy 31 (2017) 575–581.

[24] M.-H. Wu, J.-T. Lee, Y.J. Chung, M. Srinivaas, J.-M. Wu, Ultrahigh efficient degradation activity of single- and few-layered MoSe2 nanoflowers in dark by piezo-catalyst effect, Nano Energy 40 (2017) 369–375.

[25] Y. Wang, X.R. Wen, Y.M. Jia, M. Huang, F.F. Wang, X.H. Zhang, Y.Y. Bai, G. L. Yuan, Y.J. Wang, Piezo-catalysis for nondestructive tooth whitening, Nat. Commun. 11 (2020).

[26] P.L. Wang, X.Y. Li, S.Y. Fan, X. Chen, M.C. Qin, D. Long, M.O. Tad, S.M. Liu, Impact of oxygen vacancy occupancy on piezo-catalytic activity of BaTiO3 nanobelt, Appl. Catal. B-Environ. 279 (2020).

[27] Y. Wei, Y.W. Zhang, W. Geng, H.R. Su, M.C. Long, Efficient bifunctional piezocatalysis of Au/BiVO4 for simultaneous removal of 4-chlorophenol and Cr(VI) in water, Appl. Catal. B-Environ. 259 (2019).

[28] H.L. You, X.X. Ma, Z. Wu, L.F. Fei, X.Q. Chen, J. Yang, Y.S. Liu, Y.M. Jia, H.M. Li, F. F. Wang, H.T. Huang, Piezoelectrically/pyroelectrically-driven vibration/cold-hot energy harvesting for mechano-/pyro-bi-catalytic dye decomposition of NaNbO3 nanofibers, Nano Energy 52 (2018) 351–359.

[29] S. Li, Z. Zhao, J. Zhao, Z. Zhang, X. Li, J. Zhang, Recent advances of ferro-, piezo-, and pyroelectric nanomaterials for catalytic applications, ACS Appl. Nano Mater. 3 (2020) 1063–1079.

[30] Y.-C. Wang, J.M. Wu, Effect of controlled oxygen vacancy on H2-production through the piezocatalysis and piezophototronics of ferroelectric R3C ZnSnO3 nanowires, Adv. Funct. Mater. 30 (2020), 1907619.

[31] D.Y. Hong, W.L. Zang, X. Guo, Y.M. Fu, H.X. He, J. Sun, L.L. Xing, B.D. Liu, X. Y. Xue, High piezo-photocatalytic efficiency of CuS/ZnO nanowires using both solar and mechanical energy for degrading organic dye, ACS Appl. Mater. Inter 8 (2016) 21302–21314.

[32] Y.S. Dong, S.M. Dong, B. Liu, C.H. Yu, J. Liu, D. Yang, P.A.P. Yang, J. Lin, 2D piezoelectric Bi2MoO6 nanoribbons for GSH-enhanced sonodynamic therapy, Adv. Mater. 33 (2021), 2106838.

[33] P. Zhu, Y. Chen, J.L. Shi, Piezocatalytic tumor therapy by ultrasound-triggered and BaTiO3-mediated piezoelectricity, Adv. Mater. 32 (2020), 202001976.

[34] L.S. Li, E.A. Carter, Defect-mediated charge-carrier trapping and nonradiative recombination in WSe2 monolayers, J. Am. Chem. Soc. 141 (2019) 10451–10461.

[35] H.D. Li, Y.H. Sang, S.J. Chang, X. Huang, Y. Zhang, R.S. Yang, H.D. Jiang, H. Liu, Z. L. Wang, Enhanced ferroelectric-nanocrystal-based hybrid photocatalysis by ultrasonic-wave-generated piezophototronic effect, Nano Lett. 15 (2015) 2372–2379.

[36] C. Hu, S.C. Tu, N. Tian, T.Y. Ma, Y.H. Zhang, H.W. Huang, Photocatalysis enhanced by external fields, Angew. Chem. Int Ed. 60 (2021) 16309–16328.

[37] C. Hu, F. Chen, Y.G. Wang, N. Tian, T.Y. Ma, Y.H. Zhang, H.W. Huang, Exceptional cocatalyst-free photo-enhanced piezocatalytic hydrogen evolution of carbon nitride nanosheets from strong in-plane polarization, Adv. Mater. 33 (2021), 2101751.

[38] W. Liu, P.F. Wang, Y.H. Ao, J. Chen, X. Gao, B.H. Jia, T.Y. Ma, Directing charge transfer in a chemical-bonded BaTiO3@ReS2 schottky heterojunction for piezoelectric enhanced photocatalysis, Adv. Mater. (2022), 202202508.

[39] Y.J. Chung, C.S. Yang, J.T. Lee, G.H. Wu, J.M. Wu, Coupling effect of piezo-flexocatalytic hydrogen evolution with hybrid 1T-and 2H-phase few-layered MoSe (2)nanosheets, Adv. Energy Mater. 10 (2020).

[40] V. Wang, N. Xu, J.C. Liu, G. Tang, W.T. Geng, VASPKIT: a user-friendly interface facilitating high-throughput computing and analysis using VASP code, Comput. Phys. Commun. 267 (2021).

[41] G. Kresse, J. Furthmuller, Efficient iterative schemes for ab initio total-energy calculations using a plane-wave basis set, Phys. Rev. B 54 (1996) 11169–11186.

[42] G. Kresse, J. Furthmüller, Efficiency of ab-initio total energy calculations for metals and semiconductors using a plane-wave basis set, Comput. Mater. Sci. 6 (1996) 15–50.

[43] J.P. Perdew, K. Burke, M. Ernzerhof, Generalized gradient approximation made simple, Phys. Rev. Lett. 77 (1996) 3865–3868.

[44] P.E. Blöchl, Projector augmented-wave method, Phys. Rev. B 50 (1994) 17953–17979.

[45] H.J. Monkhorst, J.D. Pack, Special points for Brillouin-zone integrations, Phys. Rev. B 13 (1976) 5188–5192.

[46] S.K. Gupta, P.S. Ghosh, N. Pathak, R. Tewari, Nature of defects in blue light emitting CaZrO3: spectroscopic and theoretical study, RSC Adv. 5 (2015) 56526–56533.

[47] V. Wang, N. Xu, J.-C. Liu, G. Tang, W.-T. Geng, VASPKIT: A user-friendly interface facilitating high-throughput computing and analysis using VASP code, Comput. Phys. Commun. 267 (2021), 108033.

[48] Y.-C. Wang, J.M. Wu, Effect of controlled oxygen vacancy on H2–production through the piezocatalysis and piezophototronics of ferroelectric R3C ZnSnO3 nanowires, Adv. Funct. Mater. 30 (2020), 1907619.

[49] M.A. Chaika, R. Tomala, W. Strek, D. Hreniak, P. Dluzewski, K. Morawiec, P. V. Mateychenko, A.G. Fedorov, A.G. Doroshenko, S.V. Parkhomenko, K. Lesniewska-Matys, D. Podniesinski, A. Kozlowska, G. Mancardi, O.M. Vovk, Kinetics of Cr3+ to Cr4+ ion valence transformations and intra-lattice cation exchange of Cr4+ in Cr,Ca:YAG ceramics used as laser gain and passive Q-switching media, J. Chem. Phys. 151 (2019).

[50] Y.C. Yang, C. Song, F. Zeng, F. Pan, Y.N. Xie, T. Liu, V5+ ionic displacement induced ferroelectric behavior in V-doped ZnO films, Appl. Phys. Lett. 90 (2007), 242903.

[51] Y.C. Yang C. Song X.H. Wang F. Zeng F. Pan S.J. F., P.d.A.C. A., Cr-substitution-induced ferroelectric and improved piezoelectric properties of Zn1−xCrxO films J. Appl. Phys. 103 2008 074107.

[52] F. Fazeli, C.W. Sinclair, T. Bastow, The role of excess vacancies on precipitation kinetics in an Al-Mg-Sc alloy, Met. Mater. Trans. A 39a (2008) 2297–2305.

[53] L.S. Cavalcante, J.C. Sczancoski, J.W.M. Espinosa, V.R. Mastelaro, A. Michalowicz, P.S. Pizani, F.S. De Vicente, M.S. Li, J.A. Varela, E. Longo, Intense blue and green photoluminescence emissions at room temperature in barium zirconate powders, J. Alloy Compd. 471 (2009) 253–258.

[54] X. Liu, J. Zhang, X. Ma, H. Sheng, P. Feng, L. Shi, R. Hu, Y. Wang, Violet–blue up conversion photostimulated luminescence properties and first principles calculations of a novel un-doped CaZrO3 phosphor for application in optical storage, J. Alloy. Compd. 550 (2013) 451–458.

[55] K. Hkiri, H.E.A. Mohamed, M. Ben Salem, A. Kouki, M. Maaza, M. Zouaoui, Biosynthesis and characterization of CaZrO3 nanoparticles via Hyphaene thebaica: effect of preparation method on morphology, electrical, and dielectric properties, J. Mater. Sci. Mater. Electron. 31 (2020) 10018–10030.

[56] S. Singh, E. Senthil Kumar, M.S. Ramachandra Rao, Microstructural, optical and electrical properties of Cr-doped ZnO, Scr. Mater. 58 (2008) 866–869.

[57] H. Shi, H. Tan, W.-b Zhu, Z. Sun, Y. Ma, E. Wang, Electrospun Cr-doped Bi4Ti3O12/Bi2Ti2O7 heterostructure fibers with enhanced visible-light photocatalytic properties, J. Mater. Chem. A 3 (2015) 6586–6591.

[58] J. Liqiang, Q. Yichun, W. Baiqi, L. Shudan, J. Baojiang, Y. Libin, F. Wei, F. Honggang, S. Jiazhong, Review of photoluminescence performance of nano-sized semiconductor materials and its relationships with photocatalytic activity, Sol. Energy Mater. Sol. Cells 90 (2006) 1773–1787.

[59] S.M. Alay-e-Abbas, S. Nazir, S. Cottenier, A. Shaukat, Evaluation of thermodynamics, formation energetics and electronic properties of vacancy defects in CaZrO3, Sci. Rep. 7 (2017).

[60] S.L. Guo, S.N. Lai, J.M. Wu, Strain-induced ferroelectric heterostructure catalysts of hydrogen production through piezophototronic and piezoelectrocatalytic system, ACS Nano 15 (2021) 16106–16117.

[61] Y. Liu, Y. Zhang, Q. Yang, S. Niu, Z.L. Wang, Fundamental theories of piezotronics and piezo-phototronics, Nano Energy 14 (2015) 257–275.

[62] Y. Zhang, Y. Yang, Z.L. Wang, Piezo-phototronics effect on nano/microwire solar cells, Energy Environ. Sci. 5 (2012) 6850–6856.